


## Cavity Attenuators for Superconducting Qubits

Z. Wang,<sup>\*</sup> S. Shankar, Z.K. Mineev, P. Campagne-Ibarcq, A. Narla, and M.H. Devoret<sup>†</sup>  
*Department of Applied Physics, Yale University, New Haven, Connecticut 06520, USA*

 (Received 12 July 2018; revised manuscript received 30 October 2018; published 16 January 2019)

Dephasing induced by residual thermal photons in the readout resonator is a leading factor limiting the coherence times of qubits in the circuit quantum electrodynamics architecture. This residual thermal photon, on the order of  $10^{-1}$ – $10^{-3}$ , is suspected to arise from noise impinging on the resonator from its input and output ports. To address this problem, we designed and tested a new type of band-pass microwave attenuator that consists of a dissipative cavity well thermalized to the mixing chamber stage of a dilution refrigerator. By adding such a cavity attenuator in-line with a three-dimensional superconducting cavity housing a transmon qubit, we have reproducibly measured increased qubit coherence times. At base temperature, through a Hahn echo experiment, we measured  $T_{2e}/2T_1 = 1.0_{-0.1}^{+0.0}$  for two qubits over multiple cooldowns. Through noise-induced dephasing measurement, we obtained an upper bound of  $2 \times 10^{-4}$  on the residual photon population in the fundamental mode of the readout cavity, which to our knowledge is the lowest value reported so far. These results validate an effective method for protecting qubits against photon noise, which can be developed into a standard technology for quantum circuit experiments.

DOI: [10.1103/PhysRevApplied.11.014031](https://doi.org/10.1103/PhysRevApplied.11.014031)

### I. INTRODUCTION

The past two decades have witnessed an exponential increase in the coherence times of superconducting qubits [1]. Major breakthroughs include biasing a charge qubit at the charge-noise-insensitive point [2], shunting the Josephson junction with a capacitance to suppress noise in charge [3–5] and flux [6,7] qubits, and shunting the junction with a superinductance to eliminate offset charge noise in a fluxonium qubit [8]. Moreover, in the circuit quantum electrodynamics (QED) architecture [9,10], it is well understood that the readout cavity modifies the electromagnetic environment of the qubit and can thus affect qubit coherence [11,12]. In recent years, for transmon qubits embedded in three-dimensional (3D) microwave cavities [13], energy relaxation times  $T_1 > 100 \mu\text{s}$  have been frequently observed [14–17]. However, in these experiments, transmon coherence times  $T_2$  are much shorter than  $2T_1$ , indicating qubit coherence is predominantly limited by pure dephasing. An outstanding question in this field is whether  $T_2 \approx 2T_1$  can be reproducibly obtained in long-lifetime superconducting qubits.

One of the main dephasing channels that limit  $T_2$  is the residual thermal photon population in the readout cavity [18–24]. In the dispersive coupling regime, due to the ac Stark effect, fluctuations in the thermal photon number of the cavity cause random shifts of the qubit transition frequency and thus contribute to qubit dephasing [25]. In

the limit of average thermal photon number  $\bar{n}_{\text{th}} \ll 1$ , the induced dephasing rate is proportional to  $\bar{n}_{\text{th}}$  [20]:

$$\Gamma_{\phi}^{\text{th}} = \frac{\bar{n}_{\text{th}} \kappa \chi^2}{\kappa^2 + \chi^2}, \quad (1)$$

where  $\kappa$  is the cavity linewidth and  $\chi$  is the dispersive shift of the qubit frequency per cavity photon. Theoretically, for a 7.5-GHz cavity mode at 20 mK,  $\bar{n}_{\text{th}}$  is expected to be on the order of  $10^{-8}$ . However, the  $\bar{n}_{\text{th}}$  values estimated from measurements of  $\Gamma_{\phi}^{\text{th}}$  in recent experiments range from  $6 \times 10^{-4}$  to 0.15, corresponding to effective mode temperatures between 55 and 140 mK [22–24,26–28]. Understanding the origin of excess thermal photons and reducing  $\bar{n}_{\text{th}}$  are therefore crucial to increasing the qubit coherence times and reliably achieving  $T_2 \approx 2T_1$ .

One source of the excess  $\bar{n}_{\text{th}}$  is the coupling of the cavity mode to the input and output ports. This coupling opens a channel for auxiliary components in the microwave wiring to affect the temperature of the cavity mode. Examples of such components include commercial cryogenic attenuators, filters, and isolators. These components and the Teflon insulator in the coaxial cables are difficult to thermalize to the mixing chamber stage of the dilution fridge. Attenuators are particularly important in this regard since they are the dominant dissipation sources in the wiring of a cryostat and ideally form the bath that thermalizes the readout-cavity modes. Insulators inside commercial cryogenic attenuators have low thermal conductivities at low temperatures as do their stainless steel packages. Lately, thermal anchoring of attenuators

<sup>\*</sup>zhixin.wang@yale.edu

<sup>†</sup>michel.devoret@yale.edu

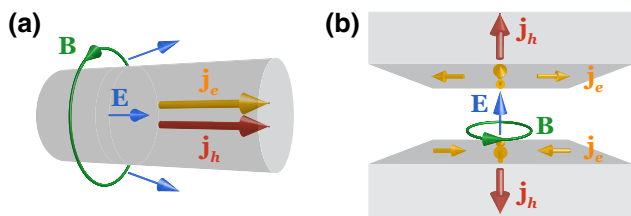


FIG. 1. Comparison of the electromagnetic fields outside and currents inside (a) a lumped-element resistor and (b) a dissipative waveguide section (TE mode). Blue and green arrows indicate electric and magnetic field lines, while yellow and red arrows indicate electric current  $\mathbf{j}_e$  and heat current  $\mathbf{j}_h$ , respectively.

has been improved by replacing these materials with better thermal conductors and redesigning the circuit layout [23]. Nevertheless, a fundamental restriction in performance arises from the lumped-element thin-film resistive network that these attenuators are made of.

An explanation of this challenge and its solution are shown in Fig. 1. In a lumped-element resistor, the electric and heat currents are parallel to each other [see Fig. 1(a)]. Given a certain electrical resistance, the order of magnitude of its thermal resistance due to electronic degrees of freedom is subject to the constraint imposed by the Wiedemann-Franz law [29]. For instance, a  $R = 50 \Omega$  resistor at 20 mK should have an electronic thermal resistance on the order of  $10^8 \text{ mK}/\mu\text{W}$ . Therefore, microwave attenuators at low temperatures are primarily thermalized through electron-phonon interaction and phonon transport [30,31]. However, this phonon mechanism suffers from a bottleneck since very few phonons are present at millikelvin temperatures. Numerical simulations show that under microwatt input power, the temperature difference inside the resistive network of the attenuator can easily reach 100 mK [23]. While it may be reduced by proper choice of materials and circuit layout, thermalizing all materials to 20 mK may be fundamentally impossible, since some thermal gradient is necessary to produce a sufficient phonon heat current.

To overcome this fundamental challenge, we would prefer to use electrons in a Fermi degenerate system to conduct heat, since electronic excitations are always present at low temperatures. We thus consider an alternative dissipation source for microwave radiation—the normal metal walls of a waveguide section. As shown in Fig. 1(b), in a dissipative waveguide, electric current mainly flows within the skin depth of the wall, while heat is conducted by electrons into the bulk metal, perpendicular to the electric current. In principle, such a distributed structure, if made of a good thermal conductor, can realize an improved cold black-body radiation environment at microwave frequencies, which is the goal of our work.

We present in this paper a narrowband microwave attenuator based on a cavity realized by a section of dissipative

waveguide, which aims at reducing the residual thermal photon population in circuit QED systems. The normal metal cavity is seamless and machined by conventional techniques without any material growth or microfabrication processes. By coupling it to a transmon-cavity system, we measured increased coherence times on two qubits in multiple cooldowns, and obtained record-breaking pure dephasing time  $T_\phi$  and  $\bar{n}_{\text{th}}$  at base temperature, leaving qubit coherence limited by energy relaxation. Because of its simple design and reliable performance, this cold cavity attenuator will provide a useful addition to the state-of-the-art quantum circuit toolbox.

## II. CAVITY ATTENUATOR DESIGN

Most commercial cryogenic attenuators have more than 10-GHz bandwidth. However, microwave pulses for qubit control and measurement are centered around only certain frequencies, and thus only narrowband attenuation is required. This forms the basis for the idea of attenuating quantum signals with a dissipative cavity. For instance, to protect a readout cavity at frequency  $f_r$  with linewidth of approximately 1 MHz from excess photon noise, we would like to supplement commercial attenuators with a cavity attenuator. Such a cavity attenuator should (1) be centered around  $f_r$ , (2) provide an attenuation of 10–20 dB on resonance, and (3) have a bandwidth of 10–50 MHz, which is an order of magnitude broader than the linewidth of the readout cavity (1–5 MHz). In addition, it should be made of a low-temperature-compatible normal metal, such as brass or, even better, oxygen-free high-thermal-conductivity (OFHC) copper.

Designing a microwave cavity that can be well thermalized to millikelvin temperatures and that has an internal dissipation rate of 10–50 MHz (internal quality factor  $Q_i \sim 500$ ) is a challenging task, since good thermal conductors also have low electrical conductor loss. Given the resistivity of the material, the quality factor of a 3D cavity resonator is approximately inversely proportional to its surface-to-volume ratio [32]. An order-of-magnitude estimate shows that the smallest dimension of our brass (OFHC copper) dissipative cavity must be in the submillimeter (sub-0.1-mm) regime. Furthermore, the on-resonance power transmission of a two-port resonator is  $4\kappa_{c1}\kappa_{c2}/(\kappa_i + \kappa_{c1} + \kappa_{c2})^2$ , where  $\kappa_i$  is the internal dissipation rate and  $\kappa_{c1}$ ,  $\kappa_{c2}$  are the external coupling rates. Attenuation of 10–20 dB requires  $\kappa_i \sim 10\kappa_{c1}$  and  $\kappa_i \sim 10\kappa_{c2}$ —the cavity being undercoupled to the couplers.

Figure 2 shows a physical realization satisfying all these requirements. It is a single-piece brass (260 alloy) block fabricated by wire electrical discharge machining (EDM) [33,34]. Such a design eliminates seams and therefore their associated loss [35]. Its external dimensions match those of the commercial WR-102 waveguides. In

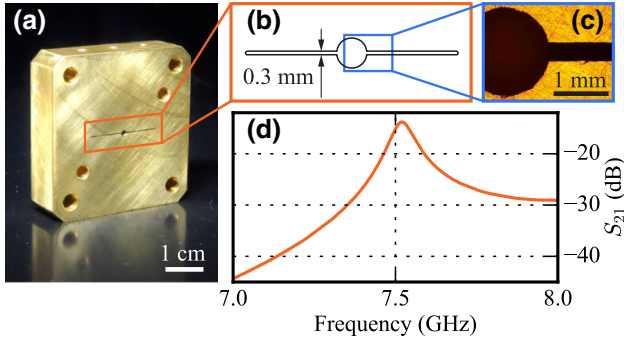


FIG. 2. Brass cavity attenuator. (a) Photograph of the device. (b) Cross-section drawing of the thin seamless cavity. (c) Enlarged optical micrograph. (d) Cavity transmission at room temperature.

addition, it can be directly thermalized to the mixing chamber of a dilution refrigerator through copper braids. As sketched in Fig. 2(b), the cavity is rectangular, apart from a cylindrical hole in the middle for starting wire EDM cutting. Because of the open boundary condition at both coupling ports, the electromagnetic field in the fundamental mode is nonuniform only in the longest dimension, which is 22 mm in this device and sets the mode frequency. The 0.3-mm gap sets the internal dissipation rate. We characterized this cavity at room temperature with a calibrated network analyzer. The waveguide couplers on both sides have  $\kappa_c \approx \kappa_i/10$ . As shown in Fig. 2(d), the transmission peak is centered at 7.52 GHz with 14-dB insertion loss. The reflection loss is 2 dB on resonance (not shown). Combined with reflection measurements, we extracted  $\kappa_i/2\pi = 54$  MHz.

On the basis of this design, we fabricated cavity attenuators with different materials and gap sizes. The parameters of three representative devices are listed in Table I. For cryogenic measurements, the temperature of the attenuator block reached 15 mK as verified by  $^{60}\text{Co}$  nuclear orientation thermometry. As seen in Table I, cavity frequencies increase due to thermal contraction at low temperature. Meanwhile, phonon vibrations freeze out, which increases the metal conductivities and reduces the cavity dissipation rates. For brass, a copper-zinc alloy,  $\kappa_i$  is reduced by approximately 20%. For OFHC copper,  $\kappa_i$  is reduced

TABLE I. Resonant frequency  $f_a$  and internal dissipation rate  $\kappa_i$  of three cavity attenuators measured at room temperature and 15 mK.

	Material	Brass	Cu	Cu
	Gap ( $\mu\text{m}$ )	300	75	125
$T = 296$ K	$f_a$ (GHz)	7.52	7.68	7.68
	$\kappa_i/2\pi$ (MHz)	54	69	62
$T = 15$ mK	$f_a$ (GHz)	7.67	7.79	7.75
	$\kappa_i/2\pi$ (MHz)	44	19	24

by a factor of about 3, indicating a tenfold increase in electrical conductivity. This value is smaller than the dc residual resistivity ratio (RRR) of OFHC copper because of the anomalous skin effect, which appears when the mean free path of the metal is longer than the wavelength of the rf-probe signal [36–38]. The dissipation rates of copper cavity attenuators are limited by the smallest diameter of the EDM cutting wires that our machine shop has access to.

### III. QUBIT COHERENCE ENHANCEMENT

We tested the performance of these cavity attenuators by coupling them to a circuit QED system and measuring the qubit coherence properties between 13 mK and 120 mK. The experimental setup is shown in Fig. 3. A cavity attenuator is connected to the sole coupling port of the aluminum cavity housing a transmon qubit. Microwave measurement of the cavity is performed in reflection. This configuration provides maximum protection against incident photon noise—the transmon is not directly exposed to any excess radiation coming from the transmission lines. Consequently, the qubit dephasing induced by thermal photons can be investigated unambiguously. However, this

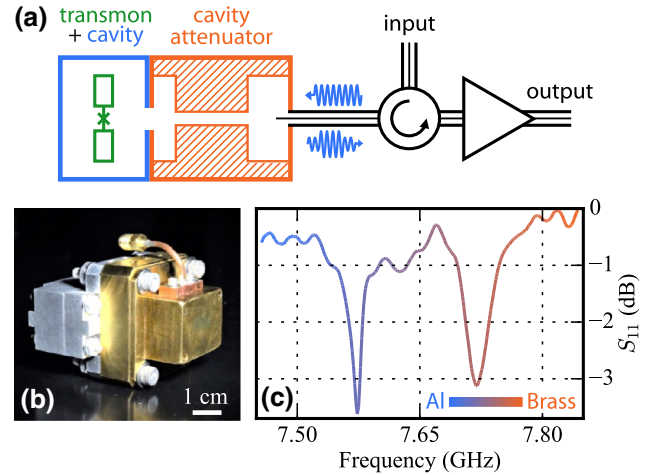


FIG. 3. Test of an attenuator with a transmon-cavity system. (a) Measurement setup anchored to the base stage of a dilution refrigerator. A transmon qubit (green) is dispersively coupled to the fundamental mode of an aluminum readout cavity (blue), which is itself coupled to a cavity attenuator (orange) through an aperture. Between the two hybridized modes, the one with greater participation in the aluminum cavity is used to measure the qubit in reflection through the standard circuit QED dispersive readout. See Fig. 8 for a detailed wiring diagram of the cryostat. (b) Photograph of the coupled cavities. The transmon is held inside the aluminum cavity (left). The cavity attenuator (middle) is coupled to the microwave lines through a coaxial cable coupler (right). See Fig. 7 for a 3D interior drawing of this assembly. (c) Cavity reflection at 13 mK showing the hybridized modes. The color bar indicates the participation of the mode in the aluminum (blue) and brass (orange) cavities.

configuration also degrades the measurement signal-to-noise ratio because the readout signal has been attenuated before being amplified by the output chain. This problem can be solved by *in situ* quantum-limited amplification, which is discussed in Sec. V. One of the ideas behind our experiment—introducing a cold dissipation source in the path of quantum signals—is similar to the idea in a previous work [27]. Alternatively, the qubit dephasing can also be suppressed by reducing the coupling rate of the readout cavity to the output line [21]. Nevertheless, compared with these strategies, our two-cavity modular approach provides more flexibility in experimental design. In addition, the cavity attenuator filters out off-resonance radiation and thus further suppresses the radiative decay of the qubit [11,12], acting as an effective Purcell filter [39].

The detailed wiring diagram of the dilution refrigerator is shown in Fig. 8. Particularly, we install 70-dB commercial cryogenic attenuators on the qubit input line, 40 dB of which are mounted on the base stage. We verified that no increase of qubit coherence times can be observed by merely increasing the attenuation of the commercial attenuators on the base stage beyond 40 dB (data not shown).

We measured the 0.3-mm-gap brass cavity attenuator coupled to a transmon–aluminum readout cavity system. The signal reflected off the combined system, measured with a network analyzer [see Fig. 3(c)], shows two hybridized modes centered at 7.573 and 7.719 GHz. Using the measured trace, we estimate that the participation of the mode centered at 7.573 GHz is 79% in the aluminum cavity and 21% in the brass cavity, while the participation of the mode centered at 7.719 GHz is 21% in the aluminum cavity and 79% in the brass cavity. We used the mode at 7.573 GHz to readout the qubit since it participates more in the aluminum cavity and thus has a larger dispersive shift. The ratio of internal dissipation to external coupling for this readout mode is estimated to be 6:1. Denoting the average photon population of the internal and external baths by  $\bar{n}_i$  and  $\bar{n}_c$ , we have  $\bar{n}_i \ll \bar{n}_c$  since the brass cavity is in thermal equilibrium with the mixing chamber. Therefore, we obtain the residual thermal population of the readout mode to be  $\bar{n}_{\text{th}} \approx \bar{n}_c/7$ , indicating 85% of residual photons are dissipated in the cold cavity attenuator.

$T_1$  and Hahn echo  $T_{2e}$  are measured as a function of temperature for two transmon-cavity systems, labeled A and B, coupled with brass and copper cavity attenuators as well as without an attenuator. As a control experiment, we also measured an aluminum filter with dimensions identical to those of the copper attenuator that, however, provides no attenuation on resonance. The transmon frequencies and anharmonicities are listed in Table II. Data taken on transmon A are shown in Figs. 4(a) and 4(b), with experimental conditions summarized in Table III. Each  $T_1$  and  $T_{2e}$  data point is the average of ten measurements performed over the course of around 1 h.

TABLE II.  $f_{ge}$  and  $\alpha = f_{ge} - f_{ef}$  (anharmonicity) of the two transmon qubits in this experiment.

Transmon	$f_{ge}$ (GHz)	$\alpha$ (GHz)
A	4.75	0.25
B	5.09	0.25

From these results we can infer that cavity attenuators dissipate excess photons in the readout mode and suppress photon-induced qubit dephasing. We see in Fig. 4(b) that  $T_{2e}$  for transmon A at base temperature is increased by more than a factor of 2 with cavity attenuators and can exceed 220  $\mu\text{s}$ . Meanwhile, Ramsey  $T_{2R}$  (not shown) is also increased, from 28–35  $\mu\text{s}$  without a cavity attenuator to 41–43  $\mu\text{s}$  with the brass attenuator and 35–40  $\mu\text{s}$

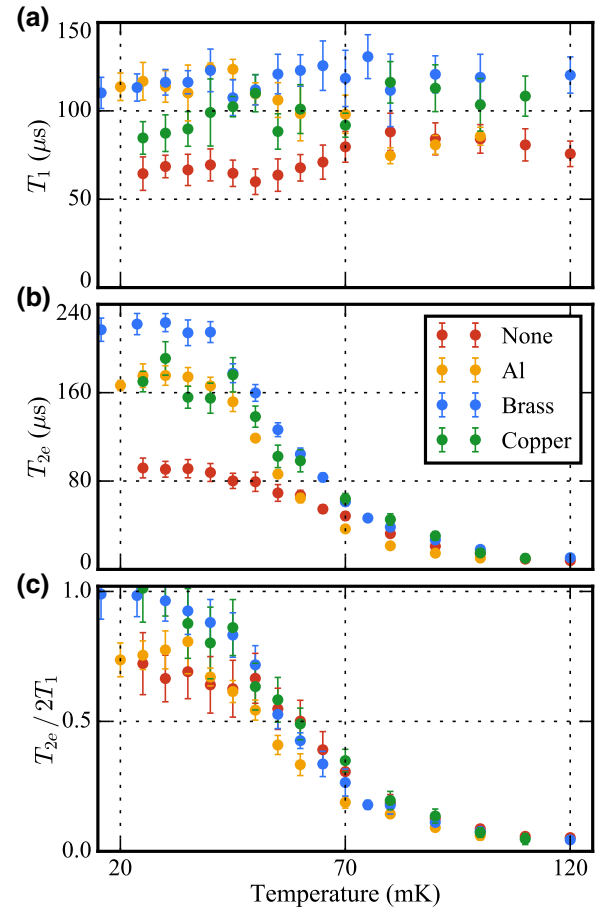


FIG. 4. Qubit coherence data. (a)  $T_1$ , (b) Hahn echo  $T_{2e}$ , and (c)  $T_{2e}/2T_1$  versus temperature with and without cavity attenuators. All the data are collected on transmon A. Error bars include both the measurement imprecision and the fluctuation of  $T_1$  over the 1 h data acquisition time. Red circles represent the data without attenuator. Yellow circles represent the data with a 75- $\mu\text{m}$ -gap aluminum cavity attenuator. Blue circles represent the data with a 300- $\mu\text{m}$ -gap brass cavity attenuator. Green circles represent the data with a 75- $\mu\text{m}$ -gap copper cavity attenuator.

TABLE III. Frequency  $f_{\text{ro}}$ , rates  $\kappa_i$  and  $\kappa_c$  of the readout mode, dispersive shift  $\chi$ ,  $T_{2e}/2T_1$ , estimated upper bounds of  $\bar{n}_{\text{th}}$  and  $T_{\text{eff}}$  at 25 mK, and transmon excited-state population  $P_e$  for each experiment in Fig. 4. The  $\kappa_i$  values for the experiments without an attenuator and with an aluminum filter are below the fitting errors.

Attenuator		$T = 25 \text{ mK}$							
Material	Gap ( $\mu\text{m}$ )	$f_{\text{ro}}$ (GHz)	$\kappa_i/2\pi$ (MHz)	$\kappa_c/2\pi$ (MHz)	$\chi/2\pi$ (MHz)	$T_{2e}/2T_1$	$\bar{n}_{\text{th}}$	$T_{\text{eff}}$ (mK)	$P_e$
None	n/a	7.573	n/a	16.5	1.5	$0.72 \pm 0.12$	$\leq 4 \times 10^{-3}$	$\leq 65$	0.01
Al	75	7.847	n/a	0.24	1.1	$0.75 \pm 0.06$	$\leq 1 \times 10^{-3}$	$\leq 55$	0.01
Brass	300	7.573	11.4	1.9	1.2	$0.98^{+0.02}_{-0.08}$	$\leq 2 \times 10^{-4}$	$\leq 43$	0.005
Cu	75	7.857	7.1	0.9	1.1	$1.00^{+0.00}_{-0.12}$	$\leq 2 \times 10^{-4}$	$\leq 44$	0.04

with the copper attenuator. The difference between  $T_{2R}$  and  $T_{2e}$  indicates that low-frequency noise in our measurement setup is causing qubit dephasing. However, since the dephasing due to residual thermal photons cannot be filtered out by a single echo pulse [21], we use  $T_{2e}$  to inform us about the effect of the cavity attenuator on the residual thermal photon population.

An important figure of merit to quantify qubit dephasing is the dimensionless value  $T_{2e}/2T_1 = T_\phi/(T_\phi + 2T_1)$ , which is close to its unity upper limit when the dephasing time satisfies  $T_\phi \gg T_1$ . As shown in Fig. 4(c), at base temperature we measured  $T_{2e}/2T_1 = 0.98^{+0.02}_{-0.08}$  with the brass attenuator. This ratio is  $1.00^{+0.00}_{-0.12}$  with the copper attenuator. In either experiment, the average  $T_\phi$  is close to 10 ms, much longer than  $T_1$ , indicating qubit coherence is limited by relaxation rather than pure dephasing. If we attribute all the qubit dephasing to the residual thermal photon population in the fundamental mode of the readout cavity, according to Eq. (1), the upper bound of  $\bar{n}_{\text{th}}$  is estimated to be on the order of  $10^{-4}$ , corresponding to an effective mode temperature  $T_{\text{eff}} \leq 40\text{--}45$  mK. As a comparison, in the absence of cavity attenuators, transmon A in the same measurement setup has  $T_\phi \approx 0.3$  ms and  $T_{2e}/2T_1 = 0.72 \pm 0.12$ , indicating  $\bar{n}_{\text{th}} \leq 4 \times 10^{-3}$  and  $T_{\text{eff}} \leq 65$  mK. The transmon excited-state populations in these experiments are measured with the protocol in Ref. [40] and listed in Table III.

To verify the efficacy of these cavity attenuators, we further performed two control experiments. First, in the same geometry as the 75- $\mu\text{m}$ -gap copper attenuator, we machined an aluminum cavity. It becomes a lossless cavity filter below 1 K and thus should leave the thermal photon population of the readout mode unchanged. By coupling it to transmon A and performing the same temperature-dependent measurements, we acquired the yellow circles in Fig. 4. At 25 mK, we measured  $T_{2e}/2T_1 = 0.75 \pm 0.06$ , indicating  $\bar{n}_{\text{th}} \leq 1 \times 10^{-3}$  and  $T_{\text{eff}} \leq 55$  mK, which are between the results without attenuator and those with the brass or copper attenuator. Therefore, we conclude that the enhancement of qubit coherence in our cavity attenuator experiments is not only due to lossless filtering, which rejects the incoming thermal photons that would populate the higher modes of the readout cavity. Dissipation

is necessary to reduce high-frequency dephasing noise caused by residual thermal photons in the readout mode.

As a second control, we repeated the copper-attenuator experiment but added to the aluminum readout cavity a copper coaxial-cable coupler with coupling rate to the readout mode of approximately 5 kHz  $\ll \kappa_c, \kappa_i$ . This input line with 70-dB cold attenuation is terminated by a  $R = 50 \Omega$  at room temperature (see Fig. 8). At 25 mK, we observed  $T_1 = 100 \pm 8 \mu\text{s}$  and  $T_{2e} = 171 \pm 10 \mu\text{s}$ , and obtained  $T_{2e}/2T_1 = 0.86 \pm 0.09$ ,  $\bar{n}_{\text{th}} \leq 1 \times 10^{-3}$ , corresponding to  $T_{\text{eff}} \leq 55$  mK (data not shown in the figures). We conclude that even a weakly coupled port has non-negligible contribution to qubit dephasing if it is not directly thermalized to the mixing chamber. On the basis of this and other experiments in our laboratory, we suspect, in particular, that the Teflon in the coaxial cable is a source of excess photons. Therefore, to achieve the best qubit coherence, ideally every coupling port on the readout cavity should be properly protected by a cold cavity attenuator.

We tested the consistency of the performance of cavity attenuators by conducting experiments on the two transmons (A and B) in multiple cooldowns. Results obtained with 300- $\mu\text{m}$ -gap brass attenuators are plotted in Fig. 5. These two cooldowns were separated by 5 months, during which time the attenuators were removed

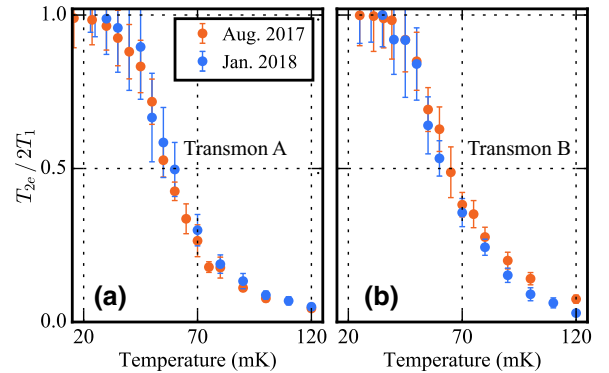


FIG. 5. Consistency of  $T_{2e}/2T_1$  across multiple samples and cooldowns when the qubits are protected by 300- $\mu\text{m}$ -gap brass cavity attenuators. For transmon B,  $T_1 \approx 50 \pm 10 \mu\text{s}$  below 100 mK.

from the setups. For both qubits, temperature-dependent measurements show good reproducibility for  $T_{2e}/2T_1$ , which is close to 1 on average and larger than 0.9 within one standard deviation at base temperature. We believe that reliable performance of these attenuators arises from their well-understood materials, structure, and fabrication process.

#### IV. THERMAL PHOTON POPULATION MEASUREMENT

Precisely measuring  $T_\phi$  and  $\bar{n}_{\text{th}}$  becomes a challenging task when  $T_2 \approx 2T_1$ , as the fluctuation of  $T_1$  over time causes the error bar of  $\Gamma_\phi = 1/T_\phi$  to exceed  $\Gamma_\phi$  itself. To mitigate the impact of the  $T_1$  fluctuation on the determination of the residual  $\bar{n}_{\text{th}}$  at base temperature, we performed noise-induced dephasing measurement on both transmons. Adopting a method similar to that in Refs. [22,24], we amplitude-modulated broadband white noise (0–80 MHz) onto a continuous-wave microwave signal at the hybridized readout frequency. The total photon population in the readout mode becomes  $n_{\text{tot}} = n_{\text{add}} + n_{\text{th}}$ ,

in which  $n_{\text{add}}$  is proportional to the output power of the noise generators. By measuring  $n_{\text{tot}}$  as a function of the noise power (see Fig. 6), we can extract  $n_{\text{th}}$  by linear regression. Finally, we obtained  $n_{\text{th}} = (2_{-2}^{+3}) \times 10^{-4}$  for transmon A and  $n_{\text{th}} = (2_{-2}^{+4}) \times 10^{-4}$  for transmon B when they were protected by copper cavity attenuators, corresponding to  $T_{\text{eff}} \leq 44\text{mK}$ . These results are consistent with the order-of-magnitude estimate in Sec. III, and lower than the values in two recent reports [23,24] that also aimed at reducing  $\bar{n}_{\text{th}}$  in circuit QED systems.

#### V. DISCUSSION

The results of our experiments have two important implications: First, cavity attenuators can reproducibly reduce  $\bar{n}_{\text{th}}$  of the readout cavity by an order of magnitude and extend  $T_{2e}$  close to the  $2T_1$  limit. Second, the improvement of qubit coherence by cavity attenuators is impacted if the readout cavity has any direct coupling to the input and output lines, even if the coupling is very weak. Our experiment suggests that excess thermal photons inevitably come from the commercial microwave components at base temperature. Consequently, cavity attenuators should be used as a standard device to create a cold black-body radiation environment for superconducting quantum circuits.

Two problems need to be solved before cavity attenuators can have broader applications in circuit QED experiments: First, in the experiments reported in this paper, qubit control and readout tones share the same coupling aperture protected by a cavity attenuator centered near the readout frequency. As a result, qubit control pulses are mostly filtered out, which slows down the qubit state manipulation. This can be avoided by separating the qubit control and readout ports and protecting them with cavity attenuators centered at different frequencies. More desirably, it is possible to design a multipole dissipative filter whose bandwidth covers a few qubits simultaneously. Second, in the current measurement setup, while dissipating excess thermal photons, the cavity attenuator also attenuates the readout signal. Consequently, the measurement signal-to-noise ratio is not sufficient for high-fidelity single-shot dispersive readout. This problem might be addressed by moving the cavity attenuator to the output port of the quantum-limited amplifier. More compactly, we could also realize *in situ* quantum-limited amplification in the readout cavity using Josephson junctions or superconducting nonlinear asymmetric inductive elements (SNAILs) [41–43]. Combined together, these solutions would bypass the conflict between the isolation and controllability of superconducting qubits, and would therefore significantly increase the qubit coherence times while retaining the benefits of strong qubit-photon interactions in artificial quantum circuits.

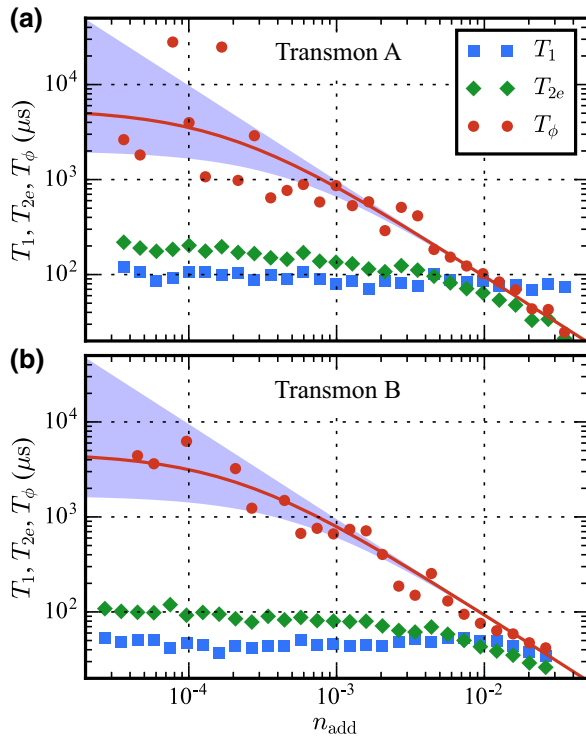


FIG. 6. Noise-induced dephasing measurement of  $\bar{n}_{\text{th}}$  in the readout mode. (a) Transmon A protected by a 75- $\mu\text{m}$ -gap copper cavity attenuator. (b) Transmon B protected by a 125- $\mu\text{m}$ -gap copper cavity attenuator.  $T_1$  (blue squares) and  $T_{2e}$  (green diamonds) are plotted versus added thermal photon number  $n_{\text{add}}$ . The extracted  $T_\phi$  values (red circles) are shown together with a fit (solid curve). Purple shading represents the fitting error within one standard deviation.

**ACKNOWLEDGMENTS**

We acknowledge insightful discussions with I. Tsioutsios and U. Vool. Use of facilities was supported by the Yale Institute for Nanoscience and Quantum Engineering (YINQE) and by the Yale School of Engineering and Applied Science clean room. This research was supported by the US Army Research Office (Grants No. W911NF-14-1-0563, No. W911NF-18-1-0020, No. W911NF-18-1-0212, No. W911NF-14-1-0011, and No. W911NF-16-1-0349) and the US Air Force Office of Scientific Research (Grant No. FA9550-15-1-0029).

**APPENDIX: EXPERIMENTAL DETAILS**

The two transmon qubits (A and B) measured in our experiments are fabricated with double-angle-evaporated Al/AIO<sub>x</sub>/Al Josephson junctions defined with use of the bridge-free electron-beam lithography technique [44,45] on double-side-polished *c*-plane sapphire chips. As depicted in Fig. 7, the transmon is placed 6.9 mm away from the center of the 3D aluminum readout cavity—an antinode of the electric field of the TE<sub>103</sub> mode, whose coupling to the qubit is intended to be minimized. The TE<sub>101</sub> mode of the readout cavity and the TE<sub>001</sub> mode of the cavity attenuator are hybridized through an aperture to form the readout mode, which is coupled to the input-output coaxial cable through a waveguide-to-SMA pin coupler. The frequency,  $\kappa_i$ , and  $\kappa_c$  of the readout mode in various experiments are listed in Table III.

As shown in Fig. 8, the coupled cavities are housed in a mu-metal (Amumetal 4K) magnetic shield with a carbon-black copper plate inside and mounted on the mixing chamber stage of a cryogen-free dilution refrigerator. The

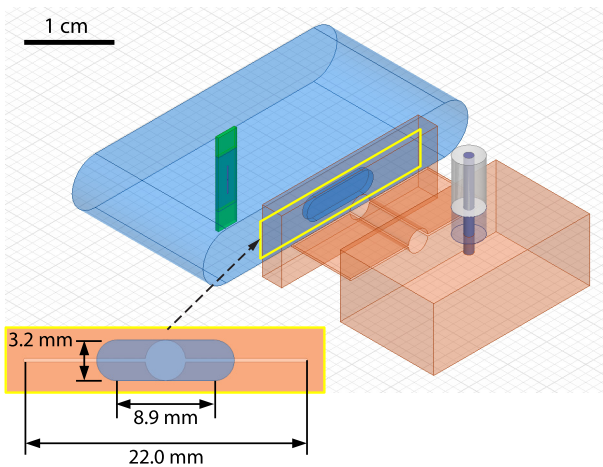


FIG. 7. Interior drawing of the readout cavity (blue)–cavity attenuator (orange)–waveguide coupler–coaxial cable assembly. The transmon qubit is on the sapphire chip (green). The enlargement is a cross-section view of the cavity attenuator and the coupling aperture between the two cavities.

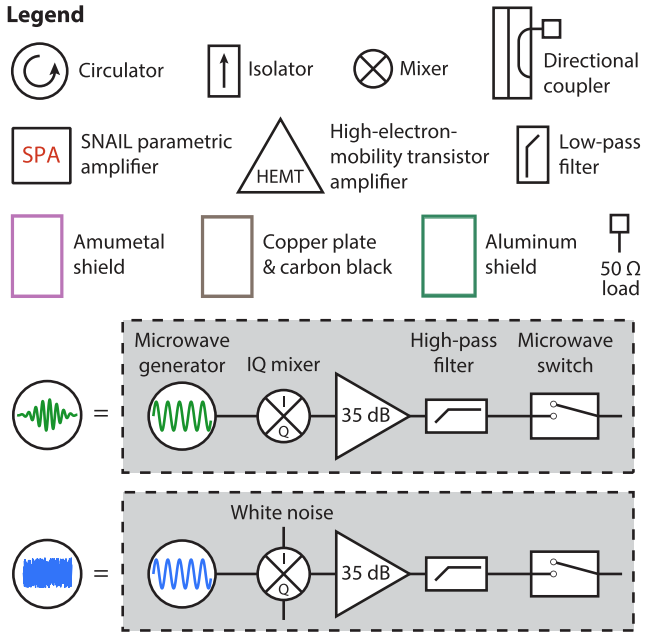
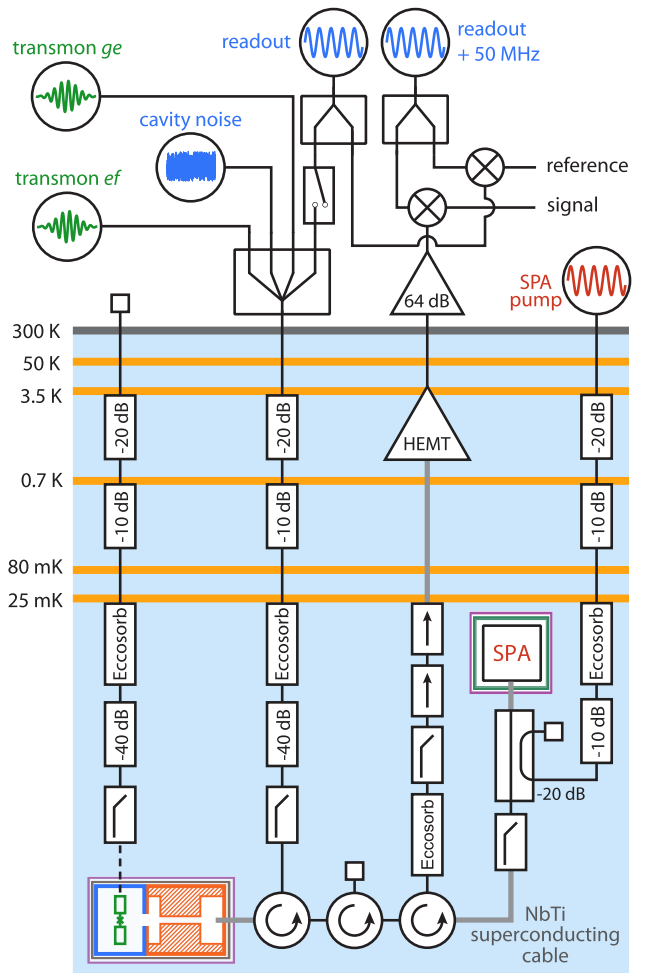


FIG. 8. Cryogenic wiring diagram with simplified room-temperature microwave electronics. The bottommost segment of the leftmost input line is dashed since it is only connected in the second control experiment reported in Sec. III.

combination of a K&L 12-GHz low-pass filter and a home-made Eccosorb filter is installed on every qubit input and output line on the base stage to block spurious radiation at high frequencies. The leftmost input line is terminated by a  $R = 50 \Omega$  load at room temperature and connected to the aluminum readout cavity through a 5-kHz coupler only in the second control experiment reported in Sec. III. A SNAIL parametric amplifier (SPA) [42,46] is used to collect part of the data sets. An array of three cryogenic circulators imposes the directionality of the readout signals, which are transmitted in NbTi superconducting cables between the cavity attenuator and the SPA, as well as between the base stage and the 3.5-K stage along the output line. The output signals are further amplified by a high-electron-mobility transistor (HEMT) amplifier at 3.5 K and a combination of room-temperature amplifiers before being demodulated by a heterodyne interferometer and digitized by an analog-to-digital card in the measurement computer.

- 
- [1] M. H. Devoret, and R. J. Schoelkopf, Superconducting circuits for quantum information: An outlook, *Science* **339**, 1169 (2013).
- [2] D. Vion, A. Aassime, A. Cottet, P. Joyez, H. Pothier, C. Urbina, D. Esteve, and M. H. Devoret, Manipulating the quantum state of an electrical circuit, *Science* **296**, 886 (2002).
- [3] A. Cottet, PhD dissertation, Universite Paris VI, 2002.
- [4] J. Koch, T. M. Yu, J. Gambetta, A. A. Houck, D. I. Schuster, J. Majer, A. Blais, M. H. Devoret, S. M. Girvin, and R. J. Schoelkopf, Charge-insensitive qubit design derived from the Cooper pair box, *Phys. Rev. A* **76**, 042319 (2007).
- [5] J. A. Schreier, A. A. Houck, J. Koch, D. I. Schuster, B. R. Johnson, J. M. Chow, J. M. Gambetta, J. Majer, L. Frunzio, M. H. Devoret, S. M. Girvin, and R. J. Schoelkopf, Suppressing charge noise decoherence in superconducting charge qubits, *Phys. Rev. B* **77**, 180502 (2008).
- [6] J. Q. You, X. Hu, S. Ashhab, and F. Nori, Low-decoherence flux qubit, *Phys. Rev. B* **75**, 140515 (2007).
- [7] M. Steffen, S. Kumar, D. P. DiVincenzo, J. R. Rozen, G. A. Keefe, M. B. Rothwell, and M. B. Ketchen, High-Coherence Hybrid Superconducting Qubit, *Phys. Rev. Lett.* **105**, 100502 (2010).
- [8] V. E. Manucharyan, J. Koch, L. I. Glazman, and M. H. Devoret, Fluxonium: Single cooper-pair circuit free of charge offsets, *Science* **326**, 113 (2009).
- [9] A. Blais, R.-S. Huang, A. Wallraff, S. M. Girvin, and R. J. Schoelkopf, Cavity quantum electrodynamics for superconducting electrical circuits: An architecture for quantum computation, *Phys. Rev. A* **69**, 062320 (2004).
- [10] A. Wallraff, D. I. Schuster, A. Blais, L. Frunzio, R.-S. Huang, J. Majer, S. Kumar, S. M. Girvin, and R. J. Schoelkopf, Strong coupling of a single photon to a superconducting qubit using circuit quantum electrodynamics, *Nature* **431**, 162 (2004).
- [11] D. Esteve, M. H. Devoret, and J. M. Martinis, Effect of an arbitrary dissipative circuit on the quantum energy levels and tunneling of a Josephson junction, *Phys. Rev. B* **34**, 158 (1986).
- [12] A. A. Houck, J. A. Schreier, B. R. Johnson, J. M. Chow, J. Koch, J. M. Gambetta, D. I. Schuster, L. Frunzio, M. H. Devoret, S. M. Girvin, and R. J. Schoelkopf, Controlling the Spontaneous Emission of a Superconducting Transmon Qubit, *Phys. Rev. Lett.* **101**, 080502 (2008).
- [13] H. Paik, D. I. Schuster, L. S. Bishop, G. Kirchmair, G. Catelani, A. P. Sears, B. R. Johnson, M. J. Reagor, L. Frunzio, L. I. Glazman, S. M. Girvin, M. H. Devoret, and R. J. Schoelkopf, Observation of High Coherence in Josephson Junction Qubits Measured in a Three-Dimensional Circuit QED Architecture, *Phys. Rev. Lett.* **107**, 240501 (2011).
- [14] D. Ristè, C. C. Bultink, M. J. Tiggelman, R. N. Schouten, K. W. Lehnert, and L. DiCarlo, Millisecond charge-parity fluctuations and induced decoherence in a superconducting transmon qubit, *Nat. Commun.* **4**, 1913 (2013).
- [15] O. Dial, D. T. McClure, S. Poletto, G. A. Keefe, M. B. Rothwell, J. M. Gambetta, D. W. Abraham, J. M. Chow, and M. Steffen, Bulk and surface loss in superconducting transmon qubits, *Supercond. Sci. Technol.* **29**, 044001 (2016).
- [16] A. Narla, S. Shankar, M. Hatridge, Z. Leghtas, K. M. Sliwa, E. Zalys-Geller, S. O. Mundhada, W. Pfaff, L. Frunzio, R. J. Schoelkopf, and M. H. Devoret, Robust Concurrent Remote Entanglement between Two Superconducting Qubits, *Phys. Rev. X* **6**, 031036 (2016).
- [17] Z. K. Mineev, S. O. Mundhada, S. Shankar, P. Reinhold, R. Gutierrez-Jauregui, R. J. Schoelkopf, M. Mirrahimi, H. J. Carmichael, and M. H. Devoret, To catch and reverse a quantum jump mid-flight, [arXiv:1803.00545](https://arxiv.org/abs/1803.00545) (2018).
- [18] P. Bertet, I. Chiorescu, G. Burkard, K. Semba, C. J. P. M. Harmans, D. P. DiVincenzo, and J. E. Mooij, Dephasing of a Superconducting Qubit Induced by Photon Noise, *Phys. Rev. Lett.* **95**, 257002 (2005).
- [19] P. Bertet, I. Chiorescu, C. J. P. M. Harmans, and J. E. Mooij, Dephasing of a flux-qubit coupled to a harmonic oscillator, [arXiv:cond-mat/0507290](https://arxiv.org/abs/cond-mat/0507290) (2005).
- [20] A. A. Clerk, and D. W. Utami, Using a qubit to measure photon-number statistics of a driven thermal oscillator, *Phys. Rev. A* **75**, 042302 (2007).
- [21] A. P. Sears, A. Petrenko, G. Catelani, L. Sun, H. Paik, G. Kirchmair, L. Frunzio, L. I. Glazman, S. M. Girvin, and R. J. Schoelkopf, Photon shot noise dephasing in the strong-dispersive limit of circuit QED, *Phys. Rev. B* **86**, 180504 (2012).
- [22] F. Yan, S. Gustavsson, A. Kamal, J. Birenbaum, A. P. Sears, D. Hover, T. J. Gudmundsen, D. Rosenberg, G. Samach, S. Weber, J. L. Yoder, T. P. Orlando, J. Clarke, A. J. Kerman, and W. D. Oliver, The flux qubit revisited to enhance coherence and reproducibility, *Nat. Commun.* **7**, 12964 (2016).
- [23] J.-H. Yeh, J. LeFebvre, S. Premaratne, F. C. Wellstood, and B. S. Palmer, Microwave attenuators for use with quantum devices below 100 mK, *J. Appl. Phys.* **121**, 224501 (2017).
- [24] F. Yan, D. Campbell, P. Krantz, M. Kjaergaard, D. Kim, J. L. Yoder, D. Hover, A. Sears, A. J. Kerman, T. P. Orlando, S. Gustavsson, and W. D. Oliver, Distinguishing Coherent and Thermal Photon Noise in a Circuit Quantum Electrodynamical System, *Phys. Rev. Lett.* **120**, 260504 (2018).



- [25] J. Gambetta, A. Blais, D. I. Schuster, A. Wallraff, L. Frunzio, J. Majer, M. H. Devoret, S. M. Girvin, and R. J. Schoelkopf, Qubit–photon interactions in a cavity: Measurement-induced dephasing and number splitting, *Phys. Rev. A* **74**, 042318 (2006).
- [26] B. Suri, Z. K. Keane, R. Ruskov, L. S. Bishop, C. Tahan, S. Novikov, J. E. Robinson, F. C. Wellstood, and B. S. Palmer, Observation of Autler–Townes effect in a dispersively dressed Jaynes–Cummings system, *New J. Phys.* **15**, 125007 (2013).
- [27] C. Rigetti, J. M. Gambetta, S. Poletto, B. L. T. Plourde, J. M. Chow, A. D. Córcoles, J. A. Smolin, S. T. Merkel, J. R. Rozen, G. A. Keefe, M. B. Rothwell, M. B. Ketchen, and M. Steffen, Superconducting qubit in a waveguide cavity with a coherence time approaching 0.1 ms, *Phys. Rev. B* **86**, 100506 (2012).
- [28] J. Goetz, S. Pogorzalek, F. Deppe, K. G. Fedorov, P. Eder, M. Fischer, F. Wulschner, E. Xie, A. Marx, and R. Gross, Photon Statistics of Propagating Thermal Microwaves, *Phys. Rev. Lett.* **118**, 103602 (2017).
- [29] N. W. Ashcroft, and N. D. Mermin, *Solid State Physics* (Cengage, Boston, 1976).
- [30] M. L. Roukes, M. R. Freeman, R. S. Germain, R. C. Richardson, and M. B. Ketchen, Hot Electrons and Energy Transport in Metals at Millikelvin Temperatures, *Phys. Rev. Lett.* **55**, 422 (1985).
- [31] F. C. Wellstood, C. Urbina, and J. Clarke, Hot-electron effects in metals, *Phys. Rev. B* **49**, 5942 (1994).
- [32] D. M. Pozar, *Microwave Engineering* (Wiley, Hoboken, 2012), 4th ed.
- [33] K. H. Ho, S. T. Newman, S. Rahimifard, and R. D. Allen, State of the art in wire electrical discharge machining (WEDM), *Int. J. Mach. Tools Manuf.* **44**, 1247 (2004).
- [34] Wire EDM cutting was performed by the Gibbs Machine Shop at Yale University and the Advanced Research Corporation (White Bear Lake, Minnesota, USA).
- [35] T. Brecht, Y. Chu, C. Axline, W. Pfaff, J. Z. Blumoff, K. Chou, L. Krayzman, L. Frunzio, and R. J. Schoelkopf, Micromachined Integrated Quantum Circuit Containing a Superconducting Qubit, *Phys. Rev. Appl.* **7**, 044018 (2017).
- [36] A. B. Pippard, The surface impedance of superconductors and normal metals at high frequencies II. the anomalous skin effect in normal metals, *Proc. Roy. Soc. A* **191**, 385 (1947).
- [37] R. G. Chambers, Anomalous skin effect in metals, *Nature* **165**, 239 (1950).
- [38] A. B. Pippard, in *Advances in Electronics and Electron Physics*, edited by L. Marton (Academic Press, New York, 1954), Vol. 6, p. 1.
- [39] M. D. Reed, B. R. Johnson, A. A. Houck, L. DiCarlo, J. M. Chow, D. I. Schuster, L. Frunzio, and R. J. Schoelkopf, Fast reset and suppressing spontaneous emission of a superconducting qubit, *Appl. Phys. Lett.* **96**, 203110 (2010).
- [40] K. Geerlings, Z. Leghtas, I. M. Pop, S. Shankar, L. Frunzio, R. J. Schoelkopf, M. Mirrahimi, and M. H. Devoret, Demonstrating a Driven Reset Protocol for a Superconducting Qubit, *Phys. Rev. Lett.* **110**, 120501 (2013).
- [41] A. Narla, K. M. Sliwa, M. Hatridge, S. Shankar, L. Frunzio, R. J. Schoelkopf, and M. H. Devoret, Wireless Josephson amplifier, *Appl. Phys. Lett.* **104**, 232605 (2014).
- [42] N. E. Frattini, U. Vool, S. Shankar, A. Narla, K. M. Sliwa, and M. H. Devoret, 3-wave mixing Josephson dipole element, *Appl. Phys. Lett.* **110**, 222603 (2017).
- [43] A. Eddins, J. M. Kreikebaum, D. M. Toyli, E. M. Levenson-Falk, A. Dove, W. P. Livingston, B. A. Levitan, L. C. G. Govia, A. A. Clerk, and I. Siddiqi, High-efficiency measurement of an artificial atom embedded in a parametric amplifier, [arXiv:1806.05276](https://arxiv.org/abs/1806.05276) (2018).
- [44] F. Lecocq, I. M. Pop, Z. Peng, I. Matei, T. Crozes, T. Fournier, C. Naud, W. Guichard, and O. Buisson, Junction fabrication by shadow evaporation without a suspended bridge, *Nanotechnology* **22**, 315302 (2011).
- [45] C. Rigetti, PhD dissertation, School Yale University, 2009.
- [46] N. E. Frattini, V. V. Sivak, A. Lingenfelter, S. Shankar, and M. H. Devoret, Optimizing the Nonlinearity and Dissipation of a SNAIL Parametric Amplifier for Dynamic Range, *Phys. Rev. Appl.* **10**, 054020 (2018).